Micron 198 (2025) 103878

Contents lists available at ScienceDirect

Micron

journal homepage: www.elsevier.com/locate/micron

Full length article

Modeling the partially detected backside reflectance of transparent substrates in reflectance microspectroscopy

Julian Schwarz [a,*], Jan Dick [a], Susanne Beuer [b], Mathias Rommel [b], Andreas Hutzler [c,*]

[a] Electron Devices, Friedrich-Alexander-Universität Erlangen-Nürnberg, Cauerstraße 6, Erlangen, 91058, Germany
[b] Fraunhofer Institute for Integrated Systems and Device Technology IISB, Schottkystraße 10, Erlangen, 91058, Germany
[c] Forschungszentrum Jülich GmbH, Helmholtz Institute Erlangen-Nürnberg for Renewable Energy (IET-2), Cauerstraße 10, Erlangen, 91058, Germany

ARTICLE INFO

Dataset link: https://doi.org/10.5281/zenodo.15342753

Keywords:
Microspectroscopy
Reflectance
Backside reflection
Transparent substrates
Thin films
Thick substrates
Incoherent layers

ABSTRACT

Thick transparent substrates are a key component for transmissive thin film optical filters and optoelectronics. In optical characterization of such substrates, light reflected from the backside — whether fully or partially detected — interferes with light directly reflected from the substrate's front side. Herein, we introduce a straightforward approach for microspectroscopic measurements, with lateral dimensions in the micrometer range, to reliably assess the amount of measured backside reflectance. Therefore, geometric calculations based on micrographs, substrate thickness and refractive index, as well as magnification of the applied objective lens are utilized as input parameters. Additionally, we account for the influence of the numerical aperture, which is essential for accurate determination of the properties of thin films coated on thick transparent substrates. Compared to simulations completely incorporating or entirely neglecting the backside reflectance, our approach significantly reduces the mean squared error between measurement and model in the case of partially detected backside reflectance. After demonstrating the capabilities of our approach to accurately identify the amount of backside reflectance detected for a variety of bare transparent substrate materials, thicknesses, and objective lenses, we prove the capacity to determine the thickness of silicon nitride and silicon nitride/silicon oxide layers on glass substrates with high consistency to complementary STEM/EDX measurements even for large numerical apertures.

1. Introduction

The measurement of reflectance using magnifying objective lenses has become established in recent years (Hutzler et al., 2017, 2019) as an alternative to state of the art techniques for thickness determination in structures with micrometer-scaled lateral dimensions, such as transmission electron microscopy (TEM) (for sufficiently transparent samples), atomic force microscopy (AFM), or specialized (microspot) ellipsometry. For this purpose, a microscope is combined with a spectrometer and allows the resolution of significantly smaller structures in the micrometer range (Schwarz et al., 2023) in contrast to conventional ellipsometry with typical measurement spot diameters from hundreds of micrometers up to a few millimeters. Various terms such as microreflectance (μReflectance) or microspectroscopy have been defined for this method (Frisenda et al., 2017; Hutzler et al., 2020).

Especially since the discovery of van der Waals materials (Novoselov et al., 2004) and the identification of their unique advantages due to their optical and electric properties (Grazianetti et al., 2024; Dutta et al., 2023; Koleśnik-Gray et al., 2023), the need for precise and reliable characterization techniques arose in the field of nanoelectronics (Zheng and Li, 2024). Besides to the so-called 2D materials, methods for the destruction-free assessment of the thickness of structured layers with lateral dimensions on the micrometer scale are essential in the semiconductor industry because of the impact of their thickness on electrical performance (He et al., 2025; Si et al., 2020).

Most van der Waals materials based devices and individual flakes are exfoliated and manufactured on a silicon substrate with a thin film of SiO_2 or related dielectrics deposited on top (Köster et al., 2022; Slavich et al., 2024a; Jeon et al., 2023), which enables compatibility with conventional microelectronics due to the common Si material platform. In the case of flakes on SiO_2/Si substrates, microspectroscopy is already a common way of characterization to determine the thickness over a large range (Schwarz et al., 2023, 2025) or to deduce the absorption down to monolayers (Mukherjee and Simsek, 2016). For material characterization, there are also investigations in which thick polymer stamps (Hsu et al., 2019; Taghavi et al., 2019) or glass (Lee

* Corresponding authors.
E-mail address: julian.schwarz@fau.de (J. Schwarz).

https://doi.org/10.1016/j.micron.2025.103878
Received 8 May 2025; Received in revised form 26 June 2025; Accepted 8 July 2025
Available online 19 July 2025

and Yee, 2021) are used as a substrate, thus enabling additional transmittance measurements in the visible spectral regime. The combined measurement of reflectance and transmittance simplifies the extraction of the complex refractive index (Mukherjee et al., 2015). Furthermore, transparent substrates are a requirement for many optical components and filters such as waveplates (Abedini Dereshgi et al., 2023; Slavich et al., 2024b) and transmissive polarizers (Moss, 2024; Zhang et al., 2024b) built upon birefringent van der Waals materials or thin films. Thick transparent substrates are also increasingly used in the field of solar cells and flexible electronics (Tiwari, 2025; Tang and Yan, 2021), enabling cheaper production via roll-to-roll processes and improving mechanical durability.

However, it is known from ellipsometry that light reflected at the backside of the substrate has a strong effect on the measurement results (Hayton and Jenkins, 2004). These reflected contributions from the backside of the substrate are also detected and interfere with the desired signal from the front surface, where for example deposited thin films provide the functionality required for the intended application. There are several approaches to suppress backside reflected light such as backside roughening, adding a material with a highly similar refractive index at the backside, diverting the backside reflected light by a wedge shape, or specialized knife-edge illumination (Funke et al., 2016; Synowicki, 2008). While roughening the rear surface or a wedge shape are no valid options if a high (specular) transmittance is required, finding a suitable material to match the refractive index without altering functionality or other properties is a challenge (Synowicki, 2008). If no suppression measures are possible, the modeling becomes more complex. In particular, due to the high angle of incidence (AOI) in ellipsometry, the light reflected from the rear side emerges from the front side with a large lateral offset (Furchner et al., 2023). This can result in only part of the rear side reflectance being detected. On the other hand, this circumstance can also be utilized by making the illumination and/or detection aperture so small that only the reflectance from the front is collected (Synowicki, 2008).

Recently, a model for ellipsometric data of a thick glass substrate was introduced considering the geometric configuration of illumination and detection, the AOI, and the substrate properties thickness and refractive index (Furchner et al., 2023). The model is based on the overlap of two circular apertures, namely the detection aperture and the displaced beam of the backside reflected light, where the lateral offset increases linearly with higher order (i.e., the multiply reflected components between the front and back of the substrate) (Furchner et al., 2023). Based on this, significant improvements were achieved for angle-resolved ellipsometry, where the back focal plane of an objective lens in a microscope setup is analyzed. In the back focal plane, the ellipsometric parameters are accessible for each AOI defined by the numerical aperture (NA). By applying the model, the accuracy to model a thin ITO film on thick glasses was drastically improved (Peng et al., 2024).

Regarding microspectroscopy, we assume that a detailed consideration of the backside reflectance is mandatory for high accuracy. This is because it can be fully, partially or not detected at all, depending on the NA, the refractive index of the substrate, its thickness, the magnification and the measurement spot size. Furthermore, we demonstrated the necessity of taking into account the influence of the NA for reflectance modeling by AOI weighting (Hutzler et al., 2020; Schwarz et al., 2023). Consequently, analysis has to be performed for each discretized AOI of the angular spectrum of the NA. A further difference of thick substrates in contrast to thin films is the occurrence of incoherence. The typical emergence of interference between the wavefronts reflected at the front and back surfaces of a thin film is typically not present for thick transparent substrates. Possible causes are loss of phase information when traveling large distances through the substrate, i.e., if the substrate is optically thicker than half of the coherence length of the light source, thickness inhomogeneities and a limited resolution of the spectrometer (Katsidis and Siapkas, 2002; Santbergen et al., 2013). Instead of a coherent superposition, the total intensity is obtained by summing the intensities of the light directly reflected at the front surface and the light reflected from the rear surface of the substrate, which passes back through the front surface upon exiting (Troparevsky et al., 2010)

Here, we expand our modular transfer matrix method (TMM) based approach established in previous works (Hutzler et al., 2020; Schwarz et al., 2023, 2025) by including incoherent layers. In addition, we introduce the PBRM model, in which we directly determine the amount of detected backside reflectance, thereby significantly increasing the accuracy of reflectance modeling. For this, we motivate an analytically straightforward solution based on literature (Furchner et al., 2023). Unlike ellipsometry, the rotationally symmetric illumination of reflected-light microscopy must be taken into account. We will demonstrate the validity of the partial backside reflectance (PBR) modeling through measurements using four objective lenses with different magnifications and NA on multiple thick transparent substrates with various material and thickness combinations. Additionally, we prove the necessity of NA correction for reliable thickness determination of thin films on top of a thick glass substrate in the form of Si_xN_y and Si_xN_y/Si_xO_y films fabricated via plasma-enhanced chemical vapor deposition (PECVD).

2. Materials and methods

2.1. Microspectroscopy

The basic structure of a microspectroscopy setup is shown in Fig. 1a. A collimated light beam is focused onto the sample by the magnifying objective lens. The reflected light obtained can be divided by a beam splitter between the camera and the spectrometer coupled by a glass fiber (Schwarz et al., 2023). A detailed description of the components is given in Section 2.1.2.

2.1.1. Reflectance modeling

The general calculation of the reflectance R_{PBRM} of a layer stack with the according layer thicknesses (t_{Sub}, t_1, and t_2 as an example for the notation for two thin layers on top of a thick substrate) exhibiting completely, partially, or not at all detected backside reflectance of the thick transparent substrate can be described by Eq. (1):

$$R_{PBRM}(\lambda) = \sum_{n=1}^{N} \Big[R_{w/,BR}(\lambda, \alpha_n) \cdot P_{PBRM}(\alpha_n) + R_{w/o,BR}(\lambda, \alpha_n) \cdot \big(1 - P_{PBRM}(\alpha_n)\big) \Big] \cdot W_{TOT}(\alpha_n), \tag{1}$$

where $R_{w/,BR}$ and $R_{w/o,BR}$ are the AOI dependent reflectance values of the layer stack with completely detected and not at all detected backside reflectance of the substrate, W_{TOT} is the objective lens dependent weighting function necessary for considering the NA, and P_{PBRM} is the ratio of detected backside reflectance, for which $0 \leq P_{PBRM} \leq 1$ applies. For NA correction, the calculation of P_{PBRM}, $R_{w/,BR}$, and $R_{w/o,BR}$ needs to be performed for each AOI α_n and, analogously to our previous work, we use $N = 50$ discretized values (Hutzler et al., 2020; Schwarz et al., 2023). The sampled values for α_n represent the discretized spectrum of AOIs provided by the objective lens or, more precisely, its NA (Schwarz et al., 2023). An elaborated derivation of the necessary number of AOIs for convergence in the simulation can be found in Section S1 of the supplementary material. W_{TOT} weights the individual reflectance spectra ($R_{w/,BR}$ and $R_{w/o,BR}$) of the corresponding α_n. The weighting comprises a geometric component solely based on the NA and an objective lens dependent parameter embodying potential inhomogeneities within the spectrum of AOIs. The formulas for α_n and W_{TOT} are explained in detail in our previous work (Schwarz et al., 2023).

For the limiting case without backside reflectance $R_{w/o,BR}$, the substrate is modeled as semi-infinite within the TMM framework, similar to the more common case of a strongly absorbing Si substrate (Schwarz

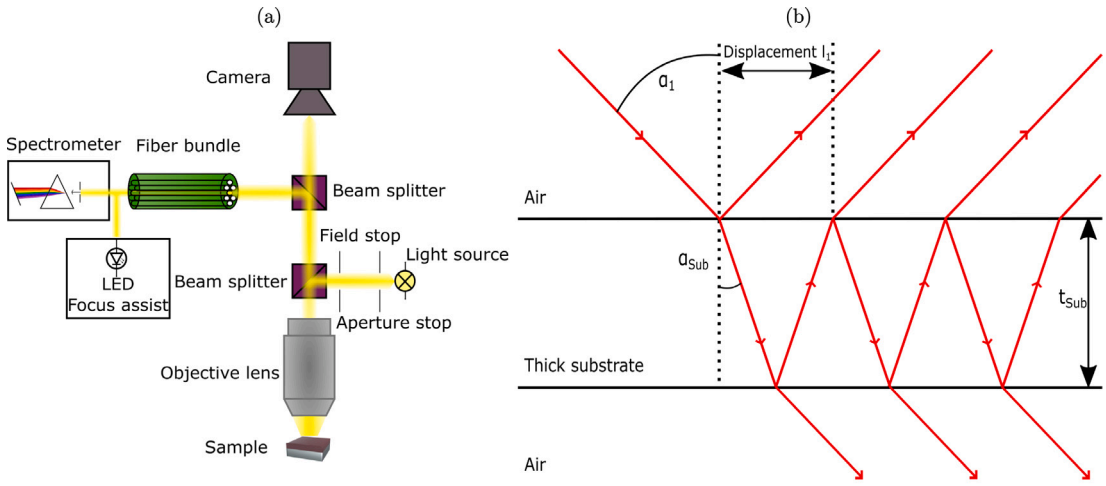

Fig. 1. (a) Microspectroscopy setup used for reflectance measurements. (b) Schematic of (multiple) reflection phenomena in (thick) transparent substrates.

et al., 2023). Then, $R_{PBRM} = R_{w/o,BR}$ as $P_{PBRM} = 0$. Vice versa, for $R_{w/,BR}$ the layer stack within the TMM must be defined in such a way that the substrate is assumed to be finite in order to take the backside reflectance into account. In that case, $R_{PBRM} = R_{w/,BR}$ and $P_{PBRM} = 1$. If a part of the backside reflectance is detected, P_{PBRM} is between 0 and 1. For modeling $R_{w/,BR}$ it is necessary to consider the thick layer (i.e., the substrate) as incoherent, so that interference fringes are replaced by the superposition of the intensity of the components reflected on the front and backside (Katsidis and Siapkas, 2002). A detailed discussion on modeling incoherent layers within the TMM algorithm is given in the last paragraph of this section. For thin films or flakes of 2D materials on top, their thickness t can be determined via minimizing the mean squared error (MSE), defined in Eq. (2), between the measured and modeled spectra by iterating over t (Schwarz et al., 2023).

$$MSE = \sum_{\lambda_{min}}^{\lambda_{max}} \frac{\left[R_{meas}(\lambda) - R_{PBRM}(\lambda)\right]^2}{M}, \tag{2}$$

Here, $R_{meas}(\lambda)$ are the measured reflectance values at each wavelength λ of the spectrum, $R_{PBRM}(\lambda)$ are the modeled reflectance values according to Eq. (1) and M is the number of measurement points within the boundaries λ_{min} and λ_{max}.

In the following, we present the mathematical and geometric fundamentals for our PBR approach. Therefore, as a starting point, Fig. 1b depicts the principle of reflected light from the front surface and light that has traversed the thick substrate and was reflected from the backside, where higher orders of multiple internal reflections are possible (Peng et al., 2024).

Under oblique incidence, there is a lateral displacement l_j of the components reflected from the backside, which is described by Eq. (3) (Furchner et al., 2023):

$$l_j(\alpha_n) = j \cdot 2 \cdot t_{Sub} \cdot \tan(\alpha_{Sub,n}), \tag{3}$$

where j is the order of the light reflected multiple times internally in the substrate, α_n is the AOI, t_{Sub} the thickness of the substrate and $\alpha_{Sub,n}$ the angle of refraction in the substrate. The angle of refraction can be determined by Snell's law in Eq. (4) (Born et al., 2019):

$$\alpha_{Sub,n} = \arcsin\left(\sin(\alpha_n) \cdot \frac{n_1}{n_{Sub}}\right). \tag{4}$$

Here, n_1 and n_{Sub} are the indices of refraction of the ambient medium (air) and the substrate. To shorten calculations, we use the average for n_{Sub} within the evaluated spectral range in Eq. (4) as the dispersion $dn/d\lambda$ is small for the investigated substrates. In contrast, the reflectance spectrum is still computed wavelength dependent within the TMM calculations. Further, we assume that only the lateral displacement in the substrate is relevant, because the displacement stemming from potential thin films on the substrate is much smaller since $t_{Film} \ll t_{Sub}$. In addition, the presence of thin films has no influence on the relation in Eq. (4) owing to its transitive nature (Born et al., 2019).

Our TMM-based approach inherently takes the contribution of all higher orders of internally reflected light into account (Born et al., 2019). For the PBR calculations, we only consider the contribution of the first order of backside reflected light and consequently only the lateral displacement l_1, illustrated in Fig. 1b, is relevant. This is justified because the higher orders are strongly attenuated by multiple internal reflections. A detailed determination of the resulting negligible inaccuracy can be found in Section S2 of the supplementary material.

The PBR approach is fundamentally based on the approach of Furchner and coworkers (Furchner et al., 2023) for ellipsometry and hence the geometric arrangement for the first order backside reflected light is schematically displayed for an arbitrary AOI in Fig. 2a. The white circle represents the position of the direct reflection at the upper boundary surface, while the blue circle represents the position of the laterally shifted first-order reflected light from the rear side at the same upper boundary surface. For the sake of simplicity, we assume that the illuminated area has the same size as the detector area and corresponds to the area of each circle. Then, the red area illustrates the overlapping area, where the highest reflectance arises. This model is valid for classical ellipsometry at a high AOI, as the lateral displacement is only present in the direction of the incident light beam (Furchner et al., 2023). Furthermore, a concentric alignment between illumination and detection apertures is presumed, similar to angle resolved ellipsometry (Peng et al., 2024).

Regarding micro(spectro)scopy, Fig. 2b shows a micrograph of a 1050 µm thick Al_2O_3 sample obtained with a 10x/NA 0.25 objective lens, where gamma correction (Bass, 1995) was applied to enhance the contrast. The illuminated area is defined by the image of the field diaphragm. In contrast to the situation shown in Fig. 2a, a radial decrease in brightness is visible. The reason for this is that in microscopy the arrangement is basically vertical and the illumination is rotationally symmetric. The lateral offset must be evaluated in all directions and hence the most overlap is located in the center and decreases radially. If the field diaphragm is fully open in Fig. 2c, the illuminated area increases and the brightness is homogeneous within the depicted region due to a drastically larger overlap region between directly reflected and backside reflected light. For reflectance measurements, however, opening the field stop is no solution, because by doing so, stray light is markedly increased and alters the measurement dramatically (see supplementary material Section S3).

Additionally, the different AOIs are caused by the use of an objective lens and defined by its NA (Katzen et al., 2018; Hutzler et al.,

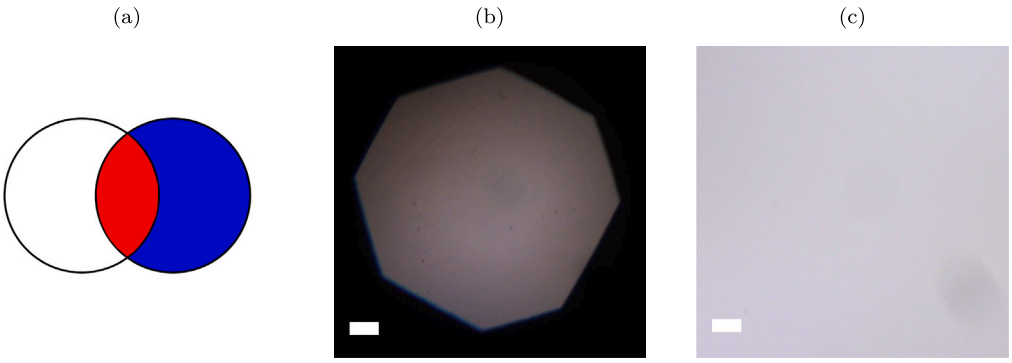

Fig. 2. (a) Sketch of the geometric constellation of the area of directly reflected (white), laterally displaced backside reflected light (blue) and the overlap region (red). (b) Section of a gamma correction adjusted micrograph of a 1050 µm thick Al_2O_3 sample obtained with a 10x/NA 0.25 objective lens. (c) Section of a micrograph of the same sample with a fully opened field diaphragm. The scale bar in (b) and (c) is 50 µm.

2020). For reflectance modeling it is necessary to consider this angular spectrum (Schwarz et al., 2023) and we need to calculate the overlap for each AOI and therefore resulting lateral displacement $l_1(\alpha_n)$. A further difference of microspectroscopy is the large disparity of diameters between the illuminated area, i.e., diameter of the directly as well as the backside reflected light, and the area of the measurement spot. In our setup, the diameter of the illuminated area exceeds the measured area by a factor of about 20. Contrary to the simplified depiction in Fig. 2a, for micro(spectro)scopy, the white circle represents the measurement spot, i.e. the detection area of the directly reflected light, and the blue circle symbolizes the area of the laterally displaced backside reflected light with a significantly larger diameter than the measurement spot. Consequently, the measured reflectance is highly dependent on the relative position of the measurement spot within the illuminated area. Beyond that, the field diaphragm is freely movable to meet the requirements for micro(spectro)scopy, so the position of the measurement spot relative to the field stop is adjustable by recentering the field diaphragm using its center alignment screws.

In the following, we introduce the procedure for calculating the overlap P_{PBRM} of the directly and first order of backside reflected light, essential for Eq. (1), of the partial backside reflectance - micro(spectro)scopy (PBRM) approach. The baseline method, termed partial backside reflectance - ellipsometry (PBRE) within this work, is based on ellipsometry (Furchner et al., 2023). A detailed derivation of the Equations for the PBRE method can be found in Section S4 of the supplementary material. The basis of operation is the overlap of two circular areas with arbitrary diameter and position in relation to each other. Applied to microspectroscopy and our PBRM approach, this overlap depends on the diameters D_{MS} of the measurement spot and the laterally displaced backside reflected light with the same diameter as the image of the field stop D_{FS}, and the distance between the centroids of the two circles. The distance is defined in terms of coordinates x_{FS}, y_{FS}, x_{MS}, y_{MS} and the AOI dependent lateral offset $l_1(\alpha_n)$. If we take into account the rotationally symmetric constellation of micro(spectro)-scopy, the lateral displacement of the light reflected at the backside must be determined in all spatial directions. The percental overlap P_{PBRM} is now evaluated as the average over the spatial directions examined according to Eq. (5):

$$
\begin{aligned}
P_{\mathrm{PBRM}}(\alpha_n) = \frac{1}{\pi^2 D_{\mathrm{MS}}} \frac{1}{\Psi} \sum_{i=0}^{i=\Psi} \Bigg[& D_{\mathrm{FS}}^2 \arccos\left(\frac{z_i(\theta_i)^2 + D_{\mathrm{FS}}^2 - D_{\mathrm{MS}}^2}{2 z_i(\theta_i) D_{\mathrm{FS}}} \right) \\
& + D_{\mathrm{MS}}^2 \arccos\left(\frac{z_i(\theta_i)^2 + D_{\mathrm{MS}}^2 - D_{\mathrm{FS}}^2}{2 z_i(\theta_i) D_{\mathrm{MS}}} \right) \\
& - \frac{1}{2} \sqrt{(D_{\mathrm{FS}} + D_{\mathrm{MS}} - z_i(\theta_i))(z_i(\theta_i) + D_{\mathrm{FS}} - D_{\mathrm{MS}})} \\
& \cdot \sqrt{(z_i(\theta_i) - D_{\mathrm{FS}} + D_{\mathrm{MS}})(z_i(\theta_i) + D_{\mathrm{FS}} + D_{\mathrm{MS}})} \Bigg] .
\end{aligned}
\tag{5}
$$

There, the lateral displacement $l_1(\alpha_n)$ is evaluated for all spatial directions θ, resulting in direction dependent coordinates $x_{i,\mathrm{BR}}$ and $y_{i,\mathrm{BR}}$ of the backside reflected light according to Eqs. (6) and (7). As a consequence, the distance between the centroids of the backside reflected light and the measurement spot z_i in Eq. (8) also depends on θ. Here, θ is quantized in 5° steps, which amounts the number of calculations Ψ to be averaged in Eq. (5) to 72.

$$x_{i,\mathrm{BR}} = x_{\mathrm{FS}} + l(\alpha_n)\cos(\theta_i) \tag{6}$$

$$y_{i,\mathrm{BR}} = y_{\mathrm{FS}} + l(\alpha_n)\sin(\theta_i) \tag{7}$$

$$z_i = \sqrt{(x_{i,\mathrm{BR}} - x_{\mathrm{MS}})^2 + (y_{i,\mathrm{BR}} - y_{\mathrm{MS}})^2} \tag{8}$$

with $\theta_i \in \{0°, 5°, 10°, \ldots, 355°\}$

The diameters D_{FS} and D_{MS} as well as the coordinates x_{FS}, y_{FS}, x_{MS}, and y_{MS} are identified from a microscope image by Python image processing based on the OpenCv module (Bradski, 2000) (see Section S5 in the supplementary material for a short description). The irregular octagon of the luminous field aperture is approximated by a circle to allow the use of Eq. (5). In Fig. 3 the measurement spot is illustrated in green, the illuminated area of the image of the field diaphragm is illustrated with a blue contour, and its circular approximation is illustrated with a red contour. Additionally, the centroids of the octagon and the circular approximation are depicted. These almost coincide, which further confirms the simplification made.

Finally, the flowchart of the PBRM procedure is schematically depicted in Fig. 3.

For modeling, the (complex) refractive indices for air (Peck and Reeder, 1972), Si (Green, 2008), SiO_2 (Hutzler et al., 2017), SiN (Vogt, 2015), Al_2O_3 (Weber, 1986), AF 32eco glass (Schott, 2025a), BF33 (Schott, 2025b), and $SrTiO_3$ (Weber, 1986) were taken from literature.

The Al_2O_3 samples are crystalline sapphire with c-plane orientation. Although our 4 × 4 TMM approach can model the birefringent behavior (Schwarz et al., 2023) of uniaxial Al_2O_3 (Weber, 1986), we assumed isotropy — based on the ordinary refractive index — because the MSE between the isotropic and anisotropic reflectance models is on the order of 10^{-9} at maximum, which is well below the noise level in our measurements. This holds even for the 100×/NA 0.9 objective lens, where the extraordinary refractive index has the largest impact due to the larger AOIs (Schwarz et al., 2023). This negligible MSE results from the weak birefringence of Al_2O_3, e.g., $\Delta n \approx 0.008$ at 500 nm.

The objective lens dependent parameter ζ of the weighting function W_{TOT}, explained in detail in Schwarz et al. (2023), were 0.3 (10x/NA 0.25), 0.7 (50xUL[1] /NA 0.35), 1.5 (100xUL[1] /NA 0.6), and 3.3 (100x/NA 0.9).

[1] 'UL' stands for 'ultra large' working distance.

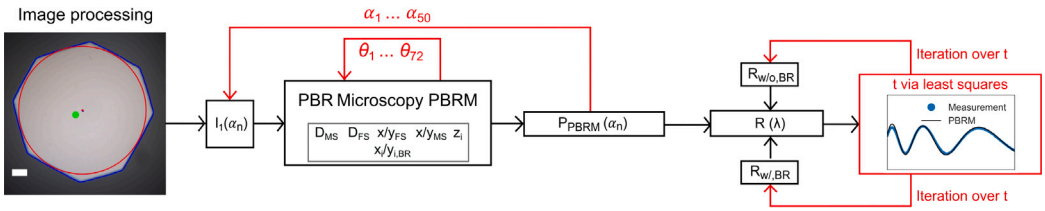

Fig. 3. Flowchart of the numerical procedure for the proposed PBRM approach. Starting from image processing (the scale bar is 50 µm), to evaluating Eq. (5) iteratively for the discretized AOIs α_n, and the iterative process of fitting the thickness t of a potential thin film on top of the substrate via minimizing least squares.

Incoherence. In literature, several techniques were introduced for modeling the reflectance and transmittance of material stacks with incoherent layer(s). An early method was the transition from the complex-valued reflection and transmission coefficients within the transfer matrices to their squared amplitudes, which leads to an intensity matrix independent of the phase difference of the directly reflected and multiply reflected wave fronts inside the thick layer (Harbecke, 1986; Katsidis and Siapkas, 2002). Another approach, based on the net radiation method, is to average the calculated reflectance values for a large number of random phase shifts added within the coherent transfer matrix of the thick layer (Santbergen et al., 2013; Troparevsky et al., 2010). However, this is computationally expensive. Further procedures are based on phase matching or phase elimination where the thickness of the thick substrate is (multiply) adjusted within the TMM simulations to achieve a vanishing sum of interference terms (Campa et al., 2013). Moreover, there is the equivalent matrix method based on calculating the necessary phase shift additions at the front and back of the incoherent layer and representing the incoherent layer with a coherent one by an equivalent propagation matrix (Puhan et al., 2017, 2019). Here, we utilize a modification of the averaging of coherent calculations with random phase shifts by applying equidistant phase shifts within an interval of π or a multiple thereof. Firstly, this reduces the number of required calculations. In our modeling, we use 9 equidistant phase values in the interval $[0, 2\pi[$, thereby suppressing the interference within the incoherent layer up to the 9th order (Santbergen et al., 2013).

Additionally, this method is capable of simulating partial coherency, i.e. the interference fringes are visible, but the amplitude is reduced. This effect usually occurs if the thickness of the layer is of the order of the coherence length of the light source and the resolution limit of the spectrometer (Santbergen et al., 2013). The modeling and measurement of a 30 µm thick AF 32eco glass (Schott, 2025a) sample showing partial coherency can be found in Section S6 of the supplementary material. At this point, we want to emphasize that partial backside reflectance and partial coherence are fundamentally different phenomena. Typically, a reduction in the visibility of the interference fringes occurs first, while the complete signal of the backside reflected light can still be detected. For thicker substrates, the interference fringes then disappear completely, and the greater lateral offset can result in only a fraction or none of the backside reflectance being collected. Depending on the constellation of illumination and detection apertures, as well as magnification and NA, there could also exist a window where both effects occur simultaneously.

2.1.2. Reflectance measurements

A sketch of the employed microspectroscopic system is presented in Fig. 1a. Our setup is based on an Olympus BX53M-TRF microscope coupled to a Horiba iHR 320 spectrometer equipped with a 1200 g/mm diffraction grating and a Horiba Synapse CCD detector. The light source is a halogen lamp and therefore the spectral range is limited from 440 nm to 950 nm. The reflectance is collected with the center fiber of a fiber bundle. The individual fibers have a diameter of 200 µm. The diameter of the circular measurement spot was determined by the magnification of the system and the diameter of the glass fiber. The four objective lenses utilized are listed in Table 1 with their NA and the resulting diameter of the measurement spot. The aperture diaphragm was fully opened to ensure the entire NA of the objective lenses was available. In contrast, the field stop was adjusted to the smallest setting to reduce stray light (Frisenda et al., 2017) and improve the signal-to-noise ratio (see Section S3 in the supplementary material). To obtain absolute reflectance values a silicon sample was used for reference measurements. The background signal containing the dark signal and noise from internal reflections in the beam path was measured on an ultra-low reflecting flock sheet from Musou Black designed for the visible and near infrared wavelength range. All spectra were averaged over 10 acquisitions.

Table 1
Objective lenses, numerical apertures and diameters of the measurement spot.

Objective lens	10x	50xUL	100xUL	100x
NA	0.25	0.35	0.60	0.90
Spot diameter/µm	20	4	2	2

2.2. Sample preparation

For this study, we investigated several transparent substrates. All samples were double side polished, thus we assumed fully specular reflection. The samples were 500 µm thick BF33 glass wafers from Schott AG, 100 µm AF 32eco thin wafers from Schott AG, 500 µm and 1050 µm thick Al_2O_3 windows from S.A.F.I.R., and 500 µm thick $SrTiO_3$ substrates from CRYSTAL GmbH. Ca. 500 nm thick Si_xN_y thin films were deposited on two BF33 wafers as single-wafer processes. On one of these wafers an additional ca. 500 nm thick Si_xO_y film was grown. The thin films were fabricated using PECVD at a deposition temperature of 130 °C. For the Si_xN_y thin film, NH_3 and SiH_4 were used as precursors. The Si_xO_y film was deposited using O_2 and SiH_4 as precursors. Both ca. 500 nm thick layers were applied in two consecutive 250 nm deposition procedures to increase the homogeneity of the layer thickness. The layers were optically measured as-deposited and did not receive any further heat treatment. Furthermore, FIB prepared TEM lamellae were analyzed by high-angle annular dark-field (HAADF)-STEM and STEM-EDX.

2.3. HAADF-STEM

STEM investigations were conducted with a Talos F200i (Thermo Fisher Scientific), equipped with a Schottky field-emission gun (X-FEG) and a Dual Bruker XFlash 6 | 100 EDX detector. A primary electron energy of 200 keV was employed for imaging and elemental analysis. The electron probe was set to a beam current of 70 pA with a convergence angle of 10.5 mrad. Elastically scattered electrons were collected using a HAADF detector within an angular range of 58 mrad to 200 mrad. Figs. 4a and b show the results of the nanoanalysis in the form of HAADF-STEM images, EDX spectrum images for oxygen and nitrogen K_{alpha} lines, and their line-wise integrated profiles for the Si_xN_y/BF33 and Si_xO_y/Si_xN_y/BF33 layer stacks. The full width at half maximum (FWHM) of the O and N signals was evaluated for the film thicknesses. For the single Si_xN_y film, the thickness is 536.4 nm and for the Si_xN_y and Si_xO_y layers in the combined stack, the thicknesses are 531.9 nm and 518.5 nm, respectively.

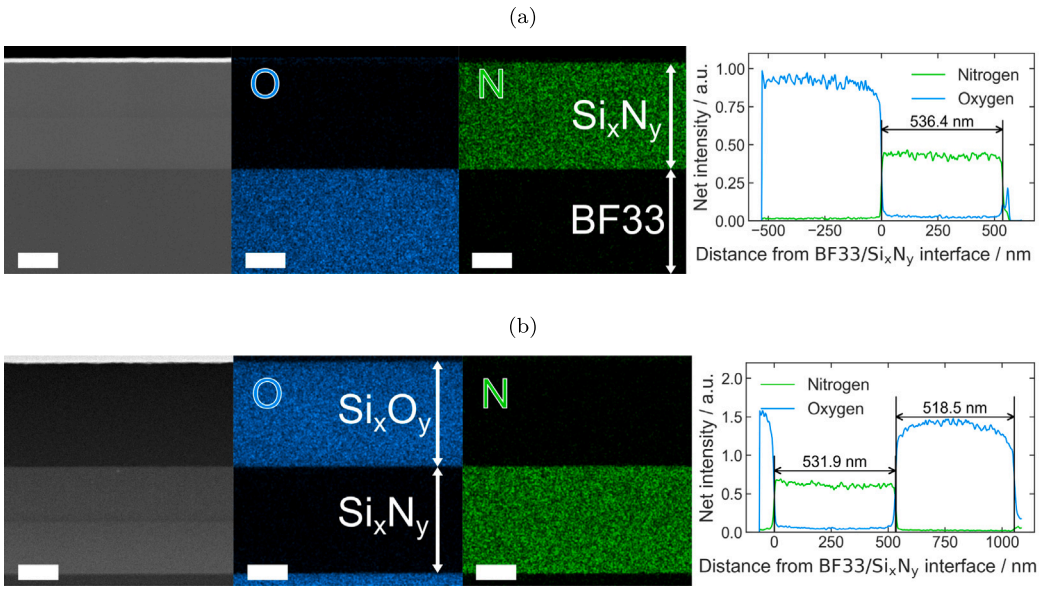

Fig. 4. HAADF-STEM images, STEM-EDX spectrum images of O and N, and corresponding line profiles of FIB lamellae for the (a) Si_xN_y/BF33 and (b) Si_xO_y/Si_xN_y/BF33 samples. For the line profiles the Si_xN_y/BF33 interface was defined as the reference point. The scale bar is 200 nm.

3. Results and discussion

3.1. Bare substrates

In the following, we present the key findings by means of representative examples. The results of all investigated substrates can be found in Section S7 in the supplementary material. If several samples of one type were available, one measurement was taken on each of two samples, labeled Meas. 1 and 2. Otherwise, only one measurement was performed. Initially, we look at instances of complete backside reflectance or lack thereof. Fig. 5a shows the measured and modeled reflectance spectra of the 500 µm thick BF33 samples obtained with the 10x/NA 0.25 objective lens. The measurements perfectly match the model with total backside reflectance (w/ BR) and our PBRM approach accurately predicts this behavior.

In contrast, the measurements of the same sample with the 50xUL/NA 0.35 objective lens in Fig. 5b exhibit nearly complete absence of backside reflectance, resembling the respective model (w/o BR). Again, the PBRM model describes this case precisely. Since the NA difference of the two objective lenses is small, the AOI distribution is comparable and thus also the lateral displacements of the backside reflected light. The difference in characteristics between Fig. 5b and Fig. 5a is due to the areas of both the backside reflected light and the measurement spot being reduced to one fifth for the 50xUL objective lens. As a consequence, there is no overlap between the measurement spot and the backside reflected light and thus only the directly reflected light is captured. In addition, for lenses with larger magnification and NA, we conclude that no rear side reflection is detected there either due to the further reduced areas or larger lateral displacement for higher AOIs.

Fig. 5c presents the results for the 100 µm thick AF 32eco sample captured with the 100xUL/NA 0.60 objective lens. The measured reflectance reveals that only a small fraction of backside reflected light was collected, but there is a clear difference to the ideal modeling without backside reflectance. Again, the PBRM approach shows excellent prediction of the measurement. As opposed to the previous findings, the slightly increased incorporation of backside reflectance is due to the smaller thickness of the AF 32eco sample, which is five times smaller than those of the BF33 samples, and the associated decreased lateral displacement of the backside reflectance. This effect outweighs the impact of the reduced diameters of the backside reflected light and the measurement spot because of the 100x magnification and the occurrence of higher AOIs stemming from the large NA of the 100xUL objective lens. The difference in refractive index of both materials has a negligible influence on deviating lateral displacement because both materials are optical glasses and the refractive index is highly similar (Schott, 2025a,b).

In summary, the modeling error MSE averaged over all investigated substrate and objective lens combinations is displayed in Fig. 5d for the individual models. These are the limiting case models with complete and without any backside reflectance and the PBRM approaches. The MSEs for the models w/ BR and w/o BR are rather high with 4.16×10^{-3} and 8.9×10^{-4}. The smaller MSE for modeling without backside reflectance in contrast to modeling with backside reflectance is due to the fact that little to no backside reflected light was measured for the two 100x objective lenses due to the small diameters of the measurement spot and laterally displaced backside reflected light. The PBRM technique reduces the error between measurements and models significantly with an averaged MSE of 1.4×10^{-5}. Herewith, the advantage of our PBR approach is obvious, and consideration of the rotationally symmetric illumination constellation of microspectroscopy results in evident improvements.

The difference between PBRM and the reference PBRE approach (results are depicted in Section S7 in the supplementary material) is rather small for these findings, since the measurement spot and the field diaphragm are nearly concentric as can be seen in Fig. 3. In other words, the measurement spot almost coincides with the centroid of the field diaphragm. In this case, the calculation of the overlap in Eq. (5) barely depends on the spatial direction and yields similar results to the baseline PBRE approach evaluated in a singular direction. Because of this, we changed the relative position of the measurement spot within the field diaphragm twice by adjusting the field diaphragm's center alignment screws and performed measurements on the 1050 µm thick Al_2O_3 sample with the 10x/NA 0.25 objective lens. The results are shown in Fig. 6 for a slightly increased distance between the centroid of the field diaphragm and the measurement as well as the measurement spot positioned in the region of the edge of the field diaphragm. A section of the micrograph including both apertures is presented as an inset respectively.

For the scenario shown in Fig. 6a, the PBRE model underestimates the measured reflectance significantly while the PBRM approach shows good agreement. In the case of the measurement spot near the edge of the field stop in Fig. 6b the model based on PBRE predicts nearly no

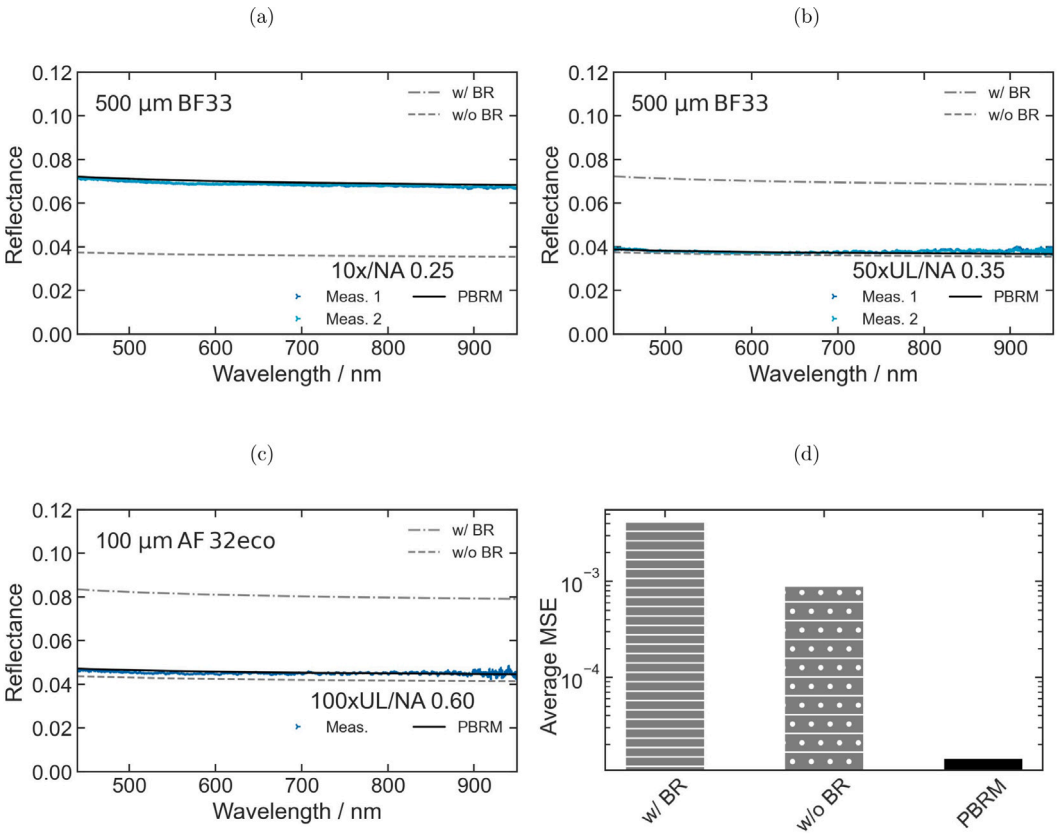

Fig. 5. Measured and modeled reflectance spectra for a 500 µm thick BF33 substrate obtained with (a) a 10x/NA 0.25 and (b) 50xUL/NA 0.35 objective lens. (c) Measured and modeled reflectance spectra for a 100 µm thick AF 32eco substrate obtained with a 100xUL/NA 0.60 objective lens. (d) MSE averaged over all objective lens and substrate combinations listed in Section S7 of the supplementary material, depicted for the different modeling approaches.

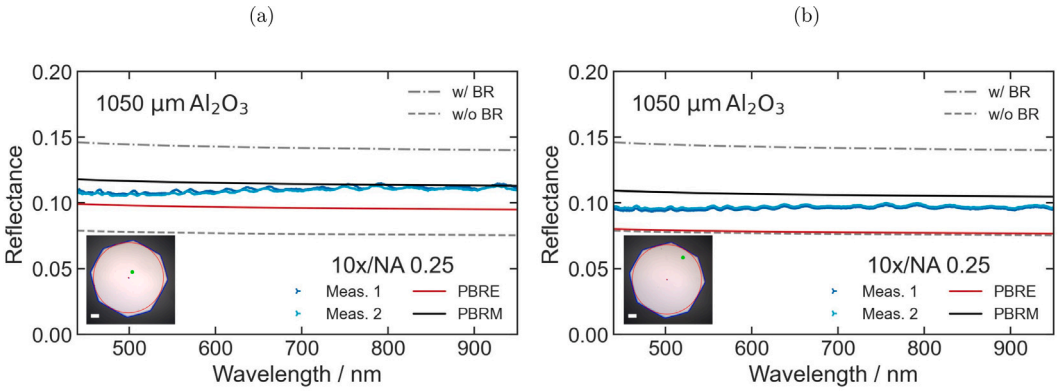

Fig. 6. Measured and modeled reflectance spectra for a 1050 µm thick Al_2O_3 substrate obtained with a 10x/NA 0.25 objective lens for different positions of the measurement spot relative to the image of the field diaphragm. Measurement spot is located (a) near the center and (b) near the edge of the illuminated area. The position of the apertures is depicted respectively as inset. The scale bar is 50 µm.

backside reflectance, whereas the PBRM forecast exhibits a much better match, albeit some deviation is visible. In terms of MSE averaged over both constellations, the PBRM approach improves the modeling by a factor of 4 with 6.6×10^{-5} compared to 2.7×10^{-4} for the PBRE based prediction.

Potential sources of error in the application of the PBR approach are inaccuracies in the determination of the position (x_{MS}, y_{MS}) and diameter D_{MS} of the measurement spot and the image of the field stop (x_{FS}, y_{FS}, D_{FS}). This also includes the approximation of a circular shape for the actual octagonal image of the field diaphragm. In image processing, variable parameters for the detection of circles and contours potentially cause uncertainties (Bradski, 2000).

3.2. Thick substrate with additional thin films

Thus far, the investigations on bare substrates show the need to consider the influence of the NA only unremarkably by a small shift in the modeled reflectance with increasing NA (see the results for each substrate and objective lens combination in Section S7 in the supplementary material). As soon as a thin film on top causes interference effects, the impact of the NA becomes more visible in the reflectance spectrum (Schwarz et al., 2023). Fig. 7a presents the measurement results for the different objective lenses of a Si_xN_y thin film on top of the BF33 substrate. From previous observations on the bare substrate, we know that the backside reflectance is completely detected for the

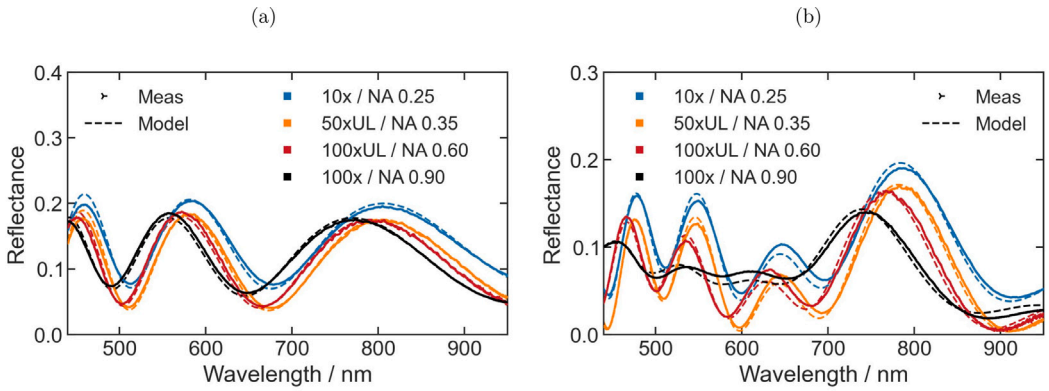

Fig. 7. Measured and modeled reflectance spectra for (a) a Si_xN_y thin film and (b) a Si_xO_y/Si_xN_y thin film stack on top of 500 µm thick BF33 substrates for different objective lenses.

10x/NA 0.25 lens and is totally absent for all other lenses. As a consequence, the corresponding limiting case models with complete ($R_{w/,BR}$) or without ($R_{w/o,BR}$) backside reflectance were used. A shift of the position of extreme points is clearly apparent with increasing NA. Besides, a decrease in amplitude emerges, especially for the 100x/NA 0.90 objective lens. Further, we see the shift in reflectance between the 10x and the higher magnifying lenses, because only the 10x lens is capable of collecting the backside reflectance. Apart from minor deviations, the modeled spectra accurately reproduce the measured ones. The determined values for thickness and MSE are presented in Table 2. These results are highly consistent between the objective lenses and are also in great accordance with the thickness of 536.4 nm from STEM-EDX spectrum imaging in Fig. 4a.

Additionally, the 'worst-case' results for thickness determination, referred to as ¬PBRM, are listed. To obtain these values, for the 10x objective lens, a complete absence of the backside reflectance was incorrectly assumed, while for the higher-magnification objective lenses, full detection of the backside reflectance was presumed. As a result, the variation in thickness for different objective lenses increases significantly, with the maximum deviation from the STEM-EDX reference value increasing from approximately 1 nm (using PBRM) to around 6 nm (using ¬PBRM). This also causes a 20- to 30-fold increase in the MSE.

To raise the complexity, we investigated a Si_xO_y/Si_xN_y/BF33 layer stack and the respective spectra are depicted in Fig. 7b. Again, the wavelength shift and diminishing amplitude range with increasing NA is observed. The modeled spectra once more reproduce the measurements with high accuracy. For the modeling in Fig. 7b, we applied the Si_xN_y thickness from the EDX study (531.9 nm) in Fig. 4b since we have no direct way of assessing the Si_xN_y layer thickness under the Si_xO_y separately via microspectroscopy. The obtained thickness and MSE values for the Si_xO_y layer are summarized in Table 2. In addition to a high level of agreement between the objective lenses, the thickness determined by STEM-EDX spectrum imaging is only slightly smaller. For both thin film stacks, additional measurements on a second sample can be found in Section S8 of the supplementary material.

The incorrect modeling using ¬PBRM also results in larger thickness variation for the Si_xO_y layer. While the MSE increases significantly — by a factor of 20 to 30 — for all objective lenses, a notable change in the determined thickness is observed only for the 100x/NA 0.9 objective lens. In this case, the striking agreement with the reference thickness determined by STEM-EDX should be considered a false positive, due to the combined factors discussed in the following paragraph. The error that occurs when determining the thickness in general highly depends on the materials involved, their thickness and the layer sequence, if the correct amount of detected reflectance of the substrate's rear side is not considered.

A source of uncertainty are the refractive indices of the PECVD prepared thin films. Such films feature a dependency on process parameters such as temperature, RF-power and frequency, pressure, flow rates of the precursors (Zhang et al., 2024a; Guler, 2019) and substrate material (Hang et al., 2020). Although the refractive indices used for the Si_xN_y film (Vogt, 2015) are eminently suitable, we used refractive indices for thermal oxide for the Si_xO_y film (Hutzler et al., 2017) because the variation in the refractive index is much smaller for PECVD deposited silicon oxides compared to silicon nitrides (Mahajan et al., 2004; Guler, 2019). The small deviation in thickness between the modeled thickness via microspectroscopy and the value from EDX may be reduced by using a dispersion model with slightly increased values of the refractive indices for the Si_xO_y film. Aside from that, there is a small window where nitrogen and oxygen overlap in the transition region between the Si_xN_y and Si_xO_y leaving the option of a small interfacial silicon oxynitride layer. This layer would have optical properties between silicon nitride and oxide (Hang et al., 2020). While implementing the interfacial layer in the modeling process is hardly possible since the exact properties (i.e., thickness, stoichiometry, and refractive index) are unknown, it is an additional small uncertainty for determining the thickness of the Si_xO_y layer.

Table 2
Comparison of thicknesses obtained from STEM-EDX spectrum imaging and microspectroscopy via the PBRM model and its opposite ¬PBRM for samples of (a) a Si_xN_y layer on a BF33 substrate and (b) the top Si_xO_y layer in a Si_xO_y/Si_xN_y stack on a BF33 substrate. In (b) the Si_xN_y thickness from the EDX study (531.9 nm) in Fig. 4b was applied. For the modeled thicknesses the MSE is denoted in brackets.

(a)

	Si_xN_y thickness/nm (MSE/10^{-5})								
Model	EDX	10x		50xUL		100xUL		100x	
PBRM	536.4	535.4	(3.3)	535.8	(2.1)	536.1	(2.3)	535.5	(2.3)
¬PBRM	536.4	537.3	(80.3)	533.5	(78.3)	533.1	(75.1)	530.3	(86.3)

(b)

	Si_xO_y thickness/nm (MSE/10^{-5})								
ID	EDX	10x		50xUL		100xUL		100x	
PBRM	518.5	524.5	(4.3)	527.4	(2.9)	526.0	(4.5)	526.6	(3.7)
¬PBRM	518.5	524.4	(123.1)	527.6	(90.5)	525.6	(97.4)	517.2	(127.9)

4. Conclusion

By calculations based on basic geometry and spatial information extracted from optical microscopy, we demonstrate the precise prediction of the amount of laterally displaced light reflected from the backside of thick transparent substrates collected in microspectroscopic reflectance measurements. Our partial backside reflectance (PBR) approach accurately reproduces the measurement for a large range of substrates and thicknesses with different objectives lenses of varying magnification and NA. We reduce the mean squared error averaged

across all samples by two to three orders of magnitude compared to the idealized modeling with completely or without detected backside reflectance. Furthermore, we show a decrease of the error by 75 % for strongly non-concentric arrangements of the measurement spot and the illuminated area by an extended PBRM model that considers the rotationally symmetric illumination constellation of microspectroscopy compared to the PBRE model based on ellipsometry. Finally, it becomes clear that the influence of NA on the measured reflectance of thin films on thick transparent substrates can also be reproduced excellently. The thicknesses obtained are highly consistent for all objective lenses used and confirm complementary STEM-EDX measurements for Si_xN_y and Si_xO_y/Si_xN_y stacks on thick substrates.

Without the introduced PBR approach, uncertainties stemming from the unconsidered partially detected backside reflectance of the thick substrate can influence the determined thickness of thin films on top of the substrate. Also, for the inverse procedure of extracting material properties such as the refractive index from the reflectance (Hsu et al., 2019; Lee and Yee, 2021) unconsidered influence of backside reflected light from the thick substrate could be falsely attributed to the investigated layer on top. As a result, we provide a fast, reliable, and easily implementable method for thin film inspection on transparent substrates in the fields of optical filters, optoelectronics, and material characterization. Since the 4 × 4 TMM is suitable to calculate the reflectance of optically anisotropic materials (Schwarz et al., 2023), our procedure can also work with anisotropic thin films and even birefringent substrates.

Looking at other possible use cases, the PBR technique is also applicable to microspectroscopic transmittance measurements (Frisenda et al., 2017; Slavich et al., 2024a), where transmitted wave fronts also experience a large lateral displacement. Especially, for high NA measurements our approach can help predicting the angular spectrum of light collected within the measurement spot on the micrometer scale.

CRediT authorship contribution statement

Julian Schwarz: Writing – review & editing, Writing – original draft, Visualization, Software, Methodology, Investigation, Formal analysis, Data curation, Conceptualization. **Jan Dick:** Writing – review & editing, Investigation. **Susanne Beuer:** Writing – review & editing, Investigation. **Mathias Rommel:** Writing – review & editing, Supervision, Software, Methodology. **Andreas Hutzler:** Writing – review & editing, Supervision, Investigation, Data curation.

Funding

This research did not receive any specific grant from funding agencies in the public, commercial, or not-for-profit sectors.

Declaration of competing interest

The authors declare that they have no known competing financial interests or personal relationships that could have appeared to influence the work reported in this paper.

Appendix A. Supplementary data

Supplementary material related to this article can be found online at https://doi.org/10.1016/j.micron.2025.103878.

Data availability

The data that support the findings of this study are openly available in Zenodo at https://doi.org/10.5281/zenodo.15342753, reference number 15342753.

References

Abedini Dereshgi, S., Lee, Y.-S., Larciprete, M.C., Centini, M., Dravid, V.P., Aydin, K., 2023. Low-symmetry $\alpha-MoO_3$ heterostructures for wave plate applications in visible frequencies. Adv. Opt. Mater. 11 (7), 2202603. http://dx.doi.org/10.1002/adom.202202603.

Bass, M. (Ed.), 1995. Handbook of Optics, second ed. vol. 1, McGraw-Hill, New York, NY.

Born, M., Wolf, E., Knight, P., 2019. Principles of Optics, 7th anniversary ed. Cambridge University Press, Cambridge, http://dx.doi.org/10.1017/9781108769914.

Bradski, G., 2000. The OpenCV library. Dr. Dobb's J. Softw. Tools 25 (11), 120–125.

Campa, A., Krc, J., Topic, M., 2013. Two approaches for incoherent propagation of light in rigourous numerical simulations. Prog. Electromagn. Res. 137, 187–202. http://dx.doi.org/10.2528/PIER13010407.

Dutta, T., Yadav, N., Wu, Y., Cheng, G.J., Liang, X., Ramakrishna, S., Sbai, A., Gupta, R., Mondal, A., Hongyu, Z., Yadav, A., 2023. Electronic properties of 2D materials and their junctions. Nano Mater. Sci. http://dx.doi.org/10.1016/j.nanoms.2023.05.003.

Frisenda, R., Niu, Y., Gant, P., Molina-Mendoza, A.J., Schmidt, R., Bratschitsch, R., Liu, J., Fu, L., Dumcenco, D., Kis, A., de Lara, D.P., Castellanos-Gomez, A., 2017. Micro-reflectance and transmittance spectroscopy: a versatile and powerful tool to characterize 2D materials. J. Phys. D: Appl. Phys. 50 (7), 074002. http://dx.doi.org/10.1088/1361-6463/aa5256.

Funke, S., Miller, B., Parzinger, E., Thiesen, P., Holleitner, A.W., Wurstbauer, U., 2016. Imaging spectroscopic ellipsometry of MoS_2. J. Phys.: Condens. Matter. 28 (38), 385301. http://dx.doi.org/10.1088/0953-8984/28/38/385301.

Furchner, A., Rappich, J., Calnan, S., Hinrichs, K., Peters, S., 2023. High-sensitivity IR to UV broadband ellipsometry and transmission characterization of high-purity glasses. Thin Solid Films 774, 139819. http://dx.doi.org/10.1016/j.tsf.2023.139819.

Grazianetti, C., Molle, A., Martella, C., 2024. The future of Xenes beyond graphene: challenges and perspective. 2D Mater. 11 (4), 042005. http://dx.doi.org/10.1088/2053-1583/ad77e0.

Green, M.A., 2008. Self-consistent optical parameters of intrinsic silicon at 300K including temperature coefficients. Sol. Energy Mater. Sol. Cells 92 (11), 1305–1310. http://dx.doi.org/10.1016/j.solmat.2008.06.009.

Guler, I., 2019. Optical and structural characterization of silicon nitride thin films deposited by PECVD. Mater. Sci. Eng.: B 246, 21–26. http://dx.doi.org/10.1016/j.mseb.2019.05.024.

Hang, L., Liu, W., Xu, J., Yang, C., Zhou, S., 2020. Effects of various substrate materials on microstructural and optical properties of amorphous silicon oxynitride thin films deposited by plasma-enhanced chemical vapor deposition. Thin Solid Films 709, 138186. http://dx.doi.org/10.1016/j.tsf.2020.138186.

Harbecke, B., 1986. Coherent and incoherent reflection and transmission of multilayer structures. Appl. Phys. B 39 (3), 165–170. http://dx.doi.org/10.1007/BF00697414.

Hayton, D.J., Jenkins, T.E., 2004. On the frustration of back-surface reflection from transparent substrates in ellipsometry. Meas. Sci. Technol. 15 (2), N17. http://dx.doi.org/10.1088/0957-0233/15/2/N01.

He, M., Yao, T., Yan, X., Qiao, B., Qian, Z., Jiang, Y., Tian, M., Yang, Z., Chen, C., 2025. Effect of film thickness on phase structure of epitaxial non-doped hafnium oxide films. Micron 190, 103762. http://dx.doi.org/10.1016/j.micron.2024.103762.

Hsu, C., Frisenda, R., Schmidt, R., Arora, A., de Vasconcellos, S.M., Bratschitsch, R., van der Zant, H.S.J., Castellanos-Gomez, A., 2019. Thickness-dependent refractive index of 1L, 2L, and 3L MoS_2, $MoSe_2$, WS_2, and WSe_2. Adv. Opt. Mater. 7 (13), 1900239. http://dx.doi.org/10.1002/adom.201900239.

Hutzler, A., Fritsch, B., Matthus, C.D., Jank, M.P.M., Rommel, M., 2020. Highly accurate determination of heterogeneously stacked van-der-Waals materials by optical microspectroscopy. Sci. Rep. 10 (1), 13676. http://dx.doi.org/10.1038/s41598-020-70580-3.

Hutzler, A., Matthus, C.D., Dolle, C., Rommel, M., Jank, M.P.M., Spiecker, E., Frey, L., 2019. Large-area layer counting of two-dimensional materials evaluating the wavelength shift in visible-reflectance spectroscopy. J. Phys. Chem. C 123 (14), 9192–9201. http://dx.doi.org/10.1021/acs.jpcc.9b00957.

Hutzler, A., Matthus, C.D., Rommel, M., Frey, L., 2017. Generalized approach to design multi-layer stacks for enhanced optical detectability of ultrathin layers. Appl. Phys. Lett. 110 (2), 021909. http://dx.doi.org/10.1063/1.4973968.

Jeon, D.-Y., Joo, S., Lee, D., Hong, S., 2023. Channel thickness-dependent degradation of field-effect mobility in multilayer MoS_2 transistors. ACS Appl. Electron. Mater. http://dx.doi.org/10.1021/acsaelm.3c01461.

Katsidis, C.C., Siapkas, D.I., 2002. General transfer-matrix method for optical multilayer systems with coherent, partially coherent, and incoherent interference. Appl. Opt. 41 (19), 3978–3987. http://dx.doi.org/10.1364/AO.41.003978.

Katzen, J.M., Velický, M., Huang, Y., Drakeley, S., Hendren, W., Bowman, R.M., Cai, Q., Chen, Y., Li, L.H., Huang, F., 2018. Rigorous and accurate contrast spectroscopy for ultimate thickness determination of micrometer-sized graphene on gold and molecular sensing. ACS Appl. Mater. & Interfaces 10 (26), 22520–22528. http://dx.doi.org/10.1021/acsami.8b01208.

Koleśnik-Gray, M., Meingast, L., Siebert, M., Unbehaun, T., Huf, T., Ellrott, G., Abellán, G., Wild, S., Lloret, V., Mundloch, U., Schwarz, J., Niebauer, M., Szabo, M., Rommel, M., Hutzler, A., Hauke, F., Hirsch, A., Krstić, V., 2023. Unconventional conductivity increase in multilayer black phosphorus. Npj 2D Mater. Appl. 7 (1), 21. http://dx.doi.org/10.1038/s41699-023-00384-2.

Köster, J., Storm, A., Gorelik, T.E., Mohn, M.J., Port, F., Gonçalves, M.R., Kaiser, U., 2022. Evaluation of TEM methods for their signature of the number of layers in mono- and few-layer TMDs as exemplified by MoS_2 and $MoTe_2$. Micron 160, 103303. http://dx.doi.org/10.1016/j.micron.2022.103303.

Lee, S.Y., Yee, K.J., 2021. Black phosphorus phase retarder based on anisotropic refractive index dispersion. 2D Mater. 9 (1), 015020. http://dx.doi.org/10.1088/2053-1583/ac3a99.

Mahajan, A.M., Patil, L.S., Gautam, D.K., 2004. Influence of process parameters on the properties of TEOS-PECVD-grown SiO_2 films. Surf. Coat. Technol. 188–189, 314–318. http://dx.doi.org/10.1016/j.surfcoat.2004.08.051.

Moss, D., 2024. 2D materials for integrated optical polarizers. http://dx.doi.org/10.20944/preprints202403.1135.v1.

Mukherjee, B., Simsek, E., 2016. Plasmonics enhanced average broadband absorption of monolayer MoS_2. Plasmonics 11 (1), 285–289. http://dx.doi.org/10.1007/s11468-015-0053-9.

Mukherjee, B., Tseng, F., Gunlycke, D., Amara, K.K., Eda, G., Simsek, E., 2015. Complex electrical permittivity of the monolayer molybdenum disulfide (MoS_2) in near UV and visible. Opt. Mater. Express 5 (2), 447–455. http://dx.doi.org/10.1364/OME.5.000447.

Novoselov, K.S., Geim, A.K., Morozov, S.V., Jiang, D., Zhang, Y., Dubonos, S.V., Grigorieva, I.V., Firsov, A.A., 2004. Electric field effect in atomically thin carbon films. Science 306 (5696), 666–669. http://dx.doi.org/10.1126/science.1102896.

Peck, E.R., Reeder, K., 1972. Dispersion of air. J. Opt. Soc. Amer. A 62 (8), 958–962. http://dx.doi.org/10.1364/JOSA.62.000958.

Peng, L., Wang, J., Gao, F., Zhang, J., Zhai, W., Zhou, L., Jiang, X., 2024. Incoherent partial superposition modeling for single-shot angle-resolved ellipsometry measurement of thin films on transparent substrates. Opt. Express 32 (9), 15774–15787. http://dx.doi.org/10.1364/OE.517216.

Puhan, J., Bűrmen, Á., Tuma, T., Fajfar, I., 2017. An accurate representation of incoherent layers within one-dimensional thin-film multilayer structures with equivalent propagation matrices. IEEE Photonics J. 9 (5), 1–12. http://dx.doi.org/10.1109/JPHOT.2017.2728535.

Puhan, J., Bűrmen, Á., Tuma, T., Fajfar, I., 2019. Irradiance in mixed coherent/incoherent structures: An analytical approach. Coatings 9 (9), http://dx.doi.org/10.3390/coatings9090536.

Santbergen, R., Smets, A.H., Zeman, M., 2013. Optical model for multilayer structures with coherent, partly coherent and incoherent layers. Opt. Express 21 (S2), A262–A267. http://dx.doi.org/10.1364/OE.21.00A262.

Schott, A., 2025a. AF 32®eco Thin Glass - Data sheet. URL https://refractiveindex.info/?shelf=specs&book=SCHOTT-misc&page=AF32ECO. (Accessed 28 February 2025).

Schott, A., 2025b. BOROFLOAT® 33 – Data sheet. URL https://media.schott.com/api/public/content/cda43a92330145c9b34db0373098ec32?v=87d55030&download=true. (Accessed 28 February 2025).

Schwarz, J., Niebauer, M., Koleśnik-Gray, M., Szabo, M., Baier, L., Chava, P., Erbe, A., Krstić, V., Rommel, M., Hutzler, A., 2023. Correlating optical microspectroscopy with 4×4 transfer matrix modeling for characterizing birefringent van der Waals materials. Small Methods 7 (10), 2300618. http://dx.doi.org/10.1002/smtd.202300618.

Schwarz, J., Niebauer, M., Römling, L., Pham, A., Koleśnik-Gray, M., Evanschitzky, P., Vogel, N., Krstić, V., Rommel, M., Hutzler, A., 2025. Spectro-spatial unmixing in optical microspectroscopy for thickness determination of layered materials. Adv. Opt. Mater. 13 (5), 2402502. http://dx.doi.org/10.1002/adom.202402502.

Si, M., Andler, J., Lyu, X., Niu, C., Datta, S., Agrawal, R., Ye, P.D., 2020. Indium-tin-oxide transistors with one nanometer thick channel and ferroelectric gating. ACS Nano 14 (9), 11542–11547. http://dx.doi.org/10.1021/acsnano.0c03978.

Slavich, A.S., Ermolaev, G.A., Tatmyshevskiy, M.K., Toksumakov, A.N., Matveeva, O.G., Grudinin, D.V., Voronin, K.V., Mazitov, A., Kravtsov, K.V., Syuy, A.V., Tsymbarenko, D.M., Mironov, M.S., Novikov, S.M., Kruglov, I., Ghazaryan, D.A., Vyshnevyy, A.A., Arsenin, A.V., Volkov, V.S., Novoselov, K.S., 2024a. Exploring van der Waals materials with high anisotropy: geometrical and optical approaches. Light.: Sci. Appl. 13 (1), 68. http://dx.doi.org/10.1038/s41377-024-01407-3.

Slavich, A., Ermolaev, G., Zavidovskiy, I., Grudinin, D., Kravtsov, K., Tatmyshevskiy, M., Mironov, M., Toksumakov, A., Tselikov, G., Fradkin, I., Voronin, K., Povolotskiy, M., Matveeva, O., Syuy, A., Yakubovsky, D., Tsymbarenko, D., Kruglov, I., Ghazaryan, D., Novikov, S., Novoselov, K., 2024b. Anisotropic van der Waals crystal with high refractive index and transparency for UV-visible range applications. http://dx.doi.org/10.48550/arXiv.2410.08771.

Synowicki, R.A., 2008. Suppression of backside reflections from transparent substrates. Phys. Status Solidi C 5 (5), 1085–1088. http://dx.doi.org/10.1002/pssc.200777873.

Taghavi, N.S., Gant, P., Huang, P., Niehues, I., Schmidt, R., Michaelis de Vasconcellos, S., Bratschitsch, R., García-Hernández, M., Frisenda, R., Castellanos-Gomez, A., 2019. Thickness determination of MoS_2, $MoSe_2$, WS_2 and WSe_2 on transparent stamps used for deterministic transfer of 2D materials. Nano Res. 12 (7), 1691–1695. http://dx.doi.org/10.1007/s12274-019-2424-6.

Tang, G., Yan, F., 2021. Recent progress of flexible perovskite solar cells. Nano Today 39, http://dx.doi.org/10.1016/j.nantod.2021.101155.

Tiwari, J.P., 2025. Flexible perovskite solar cells: A futuristic IoTs powering solar cell technology, short review. Small Methods 9 (1), http://dx.doi.org/10.1002/smtd.202400624.

Troparevsky, M.C., Sabau, A.S., Lupini, A.R., Zhang, Z., 2010. Transfer-matrix formalism for the calculation of optical response in multilayer systems: from coherent to incoherent interference. Opt. Express 18 (24), 24715–24721. http://dx.doi.org/10.1364/OE.18.024715.

Vogt, M.R., 2015. Development of Physical Models for the Simulation of Optical Properties of Solar Cell Modules (Ph.D. thesis). Leibniz Universität Hannover, Hannover, Germany.

Weber, M.J., 1986. CRC Handbook of Laser Science and Technology. Volume 4. Optical materials, Part 2 - Properties. CRC Press Inc.,Boca Raton, FL, United States.

Zhang, J., Guo, J., Zhao, Q., Yu, L., Ye, S., Yin, H., Wang, Y., 2024a. Formation of SiO_2 thin films through plasma- enhanced chemical vapor deposition using $SiH_4/Ar/N_2O$. Thin Solid Films 797, 140348. http://dx.doi.org/10.1016/j.tsf.2024.140348.

Zhang, Y., Wu, J., Jia, L., Di Jin, Jia, B., Hu, X., Moss, D., Gong, Q., 2024b. Advanced optical polarizers based on 2D materials. Npj Nanophotonics 1 (1), 28. http://dx.doi.org/10.1038/s44310-024-00028-3.

Zheng, F., Li, L.J., 2024. Microscopic characterizations for 2D material-based advanced electronics. Micron 187, 103707. http://dx.doi.org/10.1016/j.micron.2024.103707.